

# FINITE ELEMENT SIMULATION OF THE ULTRA HIGH-PERFORMANCE CONCRETE REINFORCED NEGATIVE MOMENT ZONE OF CONTINUOUS CONCRETE BOX GIRDER AFTER SIMPLE SUPPORT

*Kexin Zhang<sup>1</sup>, Dianyue Cao<sup>1</sup>, Xiaoqing Zhu<sup>1</sup>, Guanhua Zhang<sup>2</sup>,*

*Dongsheng Guo<sup>2</sup>, Houji Zhang<sup>1</sup> and Yibo Wang<sup>1</sup>*

- 1. Shenyang Jianzhu University, School of Transportation and Geomatics Engineering, Shenyang, No.25 Hunnan Zhong Road, China; jt\_zkx@sjzu.edu.cn*
- 2. Liaoning Transportation Planning and Design Co., LTD, Research and Development Center, No. 42, Lidao Road, Shenyang, Liaoning Province, China;*

## ABSTRACT

In order to explore the improvement effect of ultra-high-performance concrete (UHPC) on the mechanical property and crack resistance in the negative moment zone of the continuous concrete box girder after simple support (CCBGSS), based on the experimental research, the finite element software was used to simulate and analyze the parameters of the reinforced beam. The variation trend of the load-deflection curve obtained from numerical simulation and experimental measurements was basically consistent. The minimum error value of the cracking load was 2.0%, and the maximum was 8.4%. The minimum error value of the ultimate load was 2.0%, and the maximum was only 4.4%. This showed that the finite element model can well simulate the stress behavior of the test beam in the whole process. When the pouring thickness of UHPC increased from 60 mm to 100 mm, the cracking load and ultimate load increased by 10.3% and 5.6% respectively. When the pouring length of UHPC increased from 1.6 m to 2.0 m, the cracking load and ultimate load increased by 18.3% and 6.5% respectively.

## KEYWORDS

Continuous concrete box girder after simple support, Negative moment zone, UHPC, Mechanical property, Crack resistance, Finite element simulation

## INTRODUCTION

As traffic becomes increasingly busy, vehicle loads continue to increase, the continuous concrete box girder after simple support (CCBGSS) bridges are gradually exposed to many problems. The most frequent one is the premature cracking of the concrete in the negative moment zone of the wet joint structure at the top of the bridge pier due to heavy traffic pressure [1-2]. Ultra-high-performance concrete (UHPC), as a new material, has excellent tensile properties, ultra-high toughness, and ultra-long durability. Compared with normal concrete, UHPC can effectively solve

the problem of cracking in the negative moment zone of CCBGSS [3-5]. With the rapid development of the computer industry, the application of numerical analysis in the field of civil engineering has become more and more extensive. Utilizing the powerful analysis and calculation ability of computer, the stress state of the structure can be reflected more accurately, and the results can guide the relevant structural tests, which can save the economic cost and time cost to a great extent [6-7].

In recent years, many scholars have used finite element software simulation and practical test results to explore and study the problems in the field of Bridges. Shao [8] and Xu [9] numerically simulated the longitudinal and lateral slip diseases and the deterioration trend of lateral stiffness of prestressed concrete curved beam bridges, and proposed corresponding solutions, which provided new possibilities for further improving the disease prevention level of prestressed concrete curved beam bridges. Chung [10] and Barth [11] used the three-dimensional nonlinear finite element analysis method to predict the ultimate load behavior of the upper structure plate of the steel string bridge, and the results showed that the finite element analysis results were in good agreement with the experimental data. Rao [12] designed and manufactured two sets of 6 parallel glued T-beams with larch as raw material, observed and evaluated the failure mode and failure mechanism of glued wood beams, and established the glulam upside T-beam model with ABAQUS finite element software to simulate the mid-span deflection, displacement at measuring point, strain and failure mechanism of the members under the same load level. The conclusions provided a theoretical reference for further study of the mechanical properties of glulam T-beam. Based on finite element theory and ANSYS software, Ling [13] conducted linear and nonlinear analyses on the force conditions of continuous nodes of simply-supported girder T-girder bridges with continuous decks under different loading conditions, and obtained the theoretical basis for the design and construction of simply-supported T-girder bridge deck pavement, which can provide references to the related personnel. Wu [14] used the finite element method to analyze the interaction between the old and new box girders as well as the effect on the structural stress state of the existing box girders, and studied the possible structural diseases of the top plate and wing plate of the existing box girders and the mechanism of their generation after widening. Their research has made an outstanding contribution to the application of finite element software in the field of bridge, so that the finite element simulation analysis has a guiding significance to the field test results and practical engineering.

In this paper, the bending test of 6 concrete box beams was carried out by using UHPC to strengthen the negative moment zone of CCBGSS locally. Then, the nonlinear analysis model was established by using ABAQUS, a large general three-dimensional finite element software. The model calculation results were compared with the data obtained from the tests to verify the reasonableness of the material constitutive relationship and the correctness of the modeling. On the premise of a good agreement between the two results, the influence of different variables on the mechanical properties of the test beam after UHPC strengthened the negative bending moment zone was continued to be explored.

## **EXPERIMENTAL SCHEME AND RESULTS**

### **Test Beam Parameters**

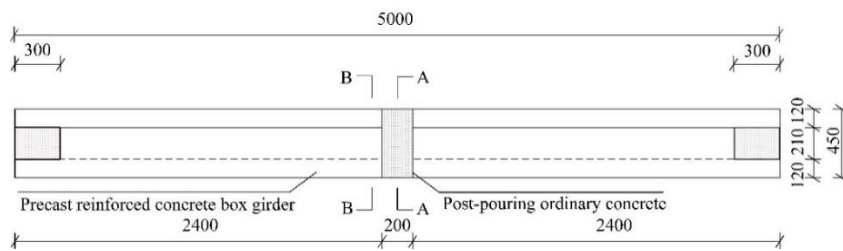
In this paper, the UHPC length, UHPC thickness and reinforcement ratio of steel bar in the

negative bending moment zone of the CCBGSS were taken as the test parameters. A total of 6 test beams were designed, one of which was a CCBGSS, and five of which were UHPC locally-reinforced CCBGSS. The parameters of each test beam are shown in Table 1, and the detailed sizes and reinforcement of the test beam are shown in Figure 1 and Figure 2.

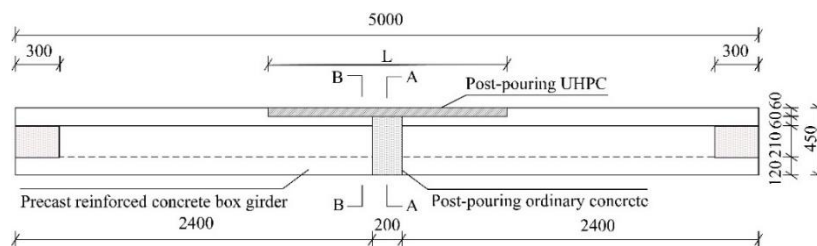
Tab. 1 - Experimental program

Test beam number	Length of UHPC (mm)	Ratio of reinforcement (%)	Thickness of UHPC (mm)
B0	—	0.43	—
B1	1600	0.36	60
B2	1600	0.43	60
B3	1600	0.50	60
B4	800	0.43	60
B5	1200	0.43	60

The pouring length of UHPC for Beams B1, B2 and B3 was all 1.6 m, and the reinforcement ratio was different, which was 0.36%, 0.43% and 0.50%, respectively. Beams B2, B4 and B5 had the same reinforcement ratio, while the pouring length of UHPC was different, which was 1.6 m, 0.8 m and 1.2 m, respectively.

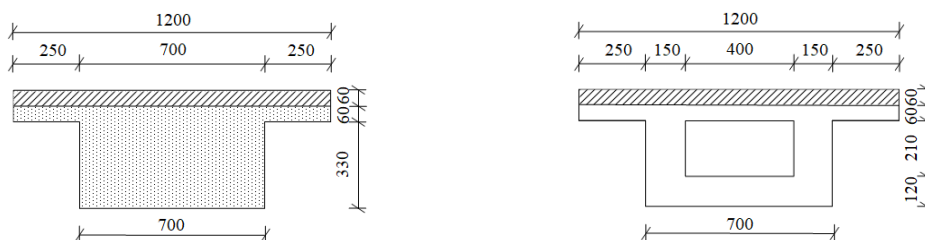


(a) - Beam B0



(b) - Beams B1, B2, B3, B4 and B5

Fig.1 - Facade diagram of test beam (unit: mm)



(a) - Cross-section of the test beam (A-A) (b) - Cross-section of the test beam (B-B)

Fig.2 - Beams B1, B2, B3, B4 and B5 (unit: mm)

### Test Beam Loading Method

This article adopted the reverse loading method to simulate the negative bending moment of the box beam. The two ends of the beam were supported on the support, and the distance between the two supports was 4600 mm. Four-point loading was used in the test, and the distance between loading points was 600 mm. The loading diagram of the test beam and the site picture are shown in Figure 3 and Figure 4.

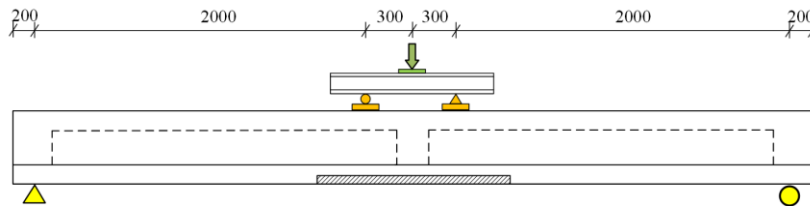


Fig.3 - Test loading diagram (unit: mm)



Fig.4 - Test site picture

### Test Results

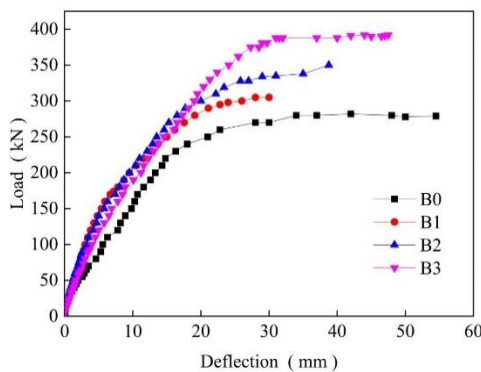


Fig.5 - Load-midspan deflection contrast curve of Beams B0, B1, B2 and B3

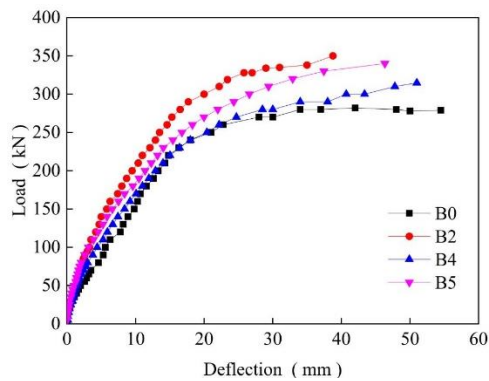


Fig.6 - Load-midspan deflection contrast curve of Beams B0, B2, B4 and B5

The load-deflection curves of CCBGSS reinforced by UHPC with different reinforcement ratios are shown in Figure 5. The cracking loads of Beams B1, B2 and B3 were significantly increased compared with Beams B0, by 35%, 46% and 54%, respectively. Beam B2 and Beam B0 had the same reinforcement ratio, due to the bridging effect of steel fibers in UHPC material, Beam B2 was significantly improved compared with Beam B0. The cracking load of Beam B1 with low reinforcement ratio still increased by 35%. As the load continued to increase, the yield load of Beam

B1 only decreased by 4% and the ultimate load increased by 8% compared with Beam B0 due to the enhancement of UHPC in the negative bending moment zone.

The load-deflection curves of UHPC reinforced CCBGSS with different UHPC pouring lengths are shown in Figure 6. The thickness of UHPC in the negative moment zone of Beams B2, B4, and B5 was 60 mm, and the lengths were 1.6 m, 0.8 m, and 1.2 m, respectively. The cracking loads of Beams B2, B4, and B5 were 95 kN, 70 kN, and 75 kN, respectively, which were significantly higher than the control Beams B0, by 46%, 8%, and 15%, respectively.

## MATERIAL PARAMETERS

### Plastic Damage Model of Concrete

ABAQUS has three types of constitutive models for concrete, including dispersion model, brittle cracking model, and plastic damage model. They have different advantages in dealing with components under different failure modes. In this paper, the plastic damage model (CDP) in ABAQUS was selected for nonlinear analysis to simulate the stiffness recovery, damage, crack development and closure behavior of concrete structural members under loads.

The plastic failure criterion of concrete damage model includes parameters such as expansion angle  $\varphi$ , eccentricity  $\varepsilon$ , strength ratio  $\sigma_{bd}/\sigma_{c0}$ ,  $K_c$ , cohesion coefficient  $\mu$  and so on, the specific values are shown in Table 2. The stress-strain curves of uniaxial compressive and tensile concrete materials in the concrete plastic damage model are shown in Figure 7 and Figure 8, respectively.

Tab. 2 - Damage model plastic failure criterion parameters

Expansion angle $\varphi$	Eccentricity $\varepsilon$	$\sigma_{bd}/\sigma_{c0}$	$K_c$	Cohesion coefficient $\mu$
30	0.1	1.16	0.667	0.0005

Note:  $\sigma_{bd}/\sigma_{c0}$  is the ratio of the ultimate compressive strength of biaxial to uniaxial,  $K$  is the ratio of the invariant,  $\mu$  is the viscosity coefficient of concrete material.

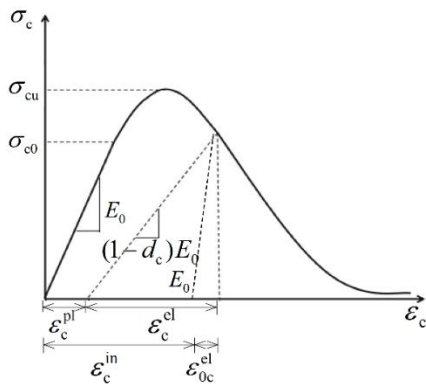


Fig. 7 - Schematic diagram of stress-strain curve of concrete under uniaxial compression

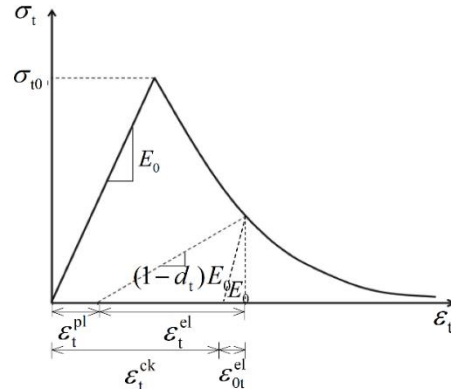


Fig. 8 - Schematic diagram of stress-strain curve of concrete under uniaxial tensile

In the figure:  $\sigma_{c0}$ —Concrete yield stress

$\sigma_{cu}$ —Ultimate stress of concrete under compression

$\sigma_{t0}$ —Tensile limit stress of concrete

$\varepsilon_c^{el}$ ,  $\varepsilon_{0c}^{el}$ —Compressive elastic strain when considering damage and no damage

$\varepsilon_c^{in}$ ,  $\varepsilon_c^{pl}$ —Inelastic strain and plastic strain of concrete under pressure

$\varepsilon_{0t}^{el}$ ,  $\varepsilon_t^{el}$ —Tensile elastic strain of concrete considering no damage and damaged

$\varepsilon_t^{ck}$ ,  $\varepsilon_t^{pl}$ —Concrete under tensile inelastic strain and plastic strain

In ABAQUS, the stress-strain relation of concrete material in plastic stage is determined by input stress-inelastic strain relation and tensile stress-inelastic strain relation. When the compressive strain of concrete exceeds the peak compressive strain, the compressive stress of concrete begins to enter the descending stage, at which time the concrete compressive stress  $\sigma_c$  and inelastic strain  $\varepsilon_c^{in}$  can be calculated by equation 1:

$$\varepsilon_c^{in} = \varepsilon_c - \sigma_c/E_c \tag{1}$$

When the tensile strain of concrete exceeds the peak tensile strain, the tensile stress of concrete material begins to decrease. The relationship between tensile stress  $\sigma_t$  and tensile cracking strain  $\varepsilon_t^{ck}$  of concrete can be calculated by equation 2.

$$\varepsilon_t^{ck} = \varepsilon_t - \sigma_t/E_t \tag{2}$$

## Tensile Constitutive Relation Curve of UHPC

Due to the UHPC material being doped with steel fibers, which gives it better tensile properties, after cracking, there is still a continuous tensile stress in the UHPC. In the axial tensile test, the UHPC specimen is mainly manifested as follows: after the specimen reaches the elastic limit tensile stress  $f_t$ , the stress decreases suddenly, but the tensile stress decreases slowly until the strain reaches about 0.2%, and then the tensile stress decreases faster. In order to describe the mechanical behavior of UHPC more accurately, the plastic section before the crack width reaches 0.3mm (the plastic strain of the axial tensile specimen is 0.2%) is simplified as a horizontal straight line, and the corresponding curve model of UHPC is shown in Figure 9.

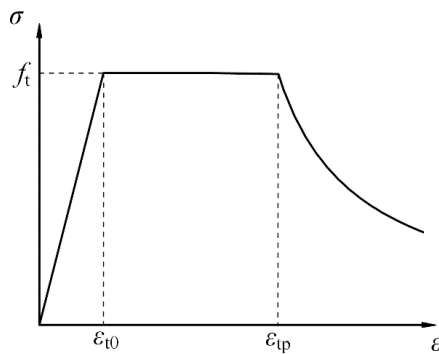


Fig.9 - Uniaxial tensile stress-strain curve of UHPC

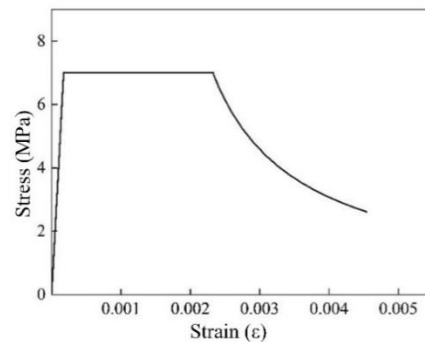


Fig.10 - Tensile constitutive curve of UHPC

The corresponding UHPC axial tension constitutive relation expression is as follows:

Elastic segment:

$$\sigma_t = \frac{f_t}{\varepsilon_{t0}} \varepsilon_t \quad (3)$$

Platform segment ( $w < 0.3$  mm):

$$\sigma_t = f_t \quad (4)$$

Softening segment ( $w \geq 0.3$  mm):

$$\sigma_t = f_t \frac{1}{p_1 \left( \frac{w}{w_0} - 1 \right)^{p_2} + \frac{w}{w_0}} \quad (5)$$

Among them,  $p_1$  and  $p_2$  are the parameters obtained by fitting, which are -0.931 and 0.949 respectively.

According to the UHPC mechanical property test results, the  $f_t$  used in this constitutive relation is the initial cracking stress of 7.79 MPa, and the endpoint  $\varepsilon$  of the flat section is taken as 2069  $\mu\varepsilon$ . The UHPC uniaxial compression stress-strain constitutive curve can be obtained by the above equation, as shown in Figure 10.

## Constitutive Modeling of Normal Concrete

### Compressive Constitutive Relation Curve of Concrete

In the finite element model of test beam, the uniaxial stress-strain constitutive relation of normal

concrete is selected in *Code for Design of Concrete Structures* (GB 50010-2010) to simulate, and the uniaxial stress-strain curve of concrete is shown in Figure 11. The uniaxial compressive stress-strain curve of C40 concrete is shown in Figure 12.

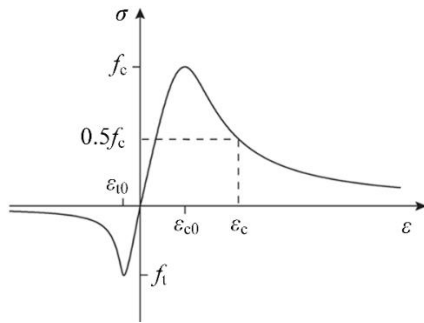


Fig. 11 - Uniaxial stress-strain curve of concrete

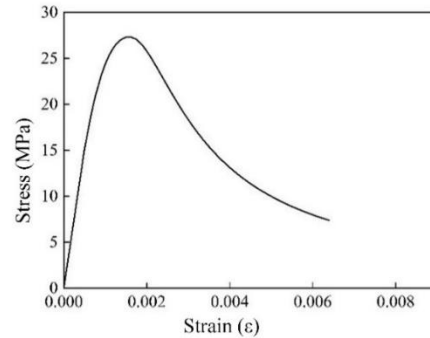


Fig. 12 - Compression constitutive curve of C40 concrete

### Tensile Constitutive Relationship Curve of Concrete

The uniaxial compressive stress-strain curve of C40 concrete is shown in Figure 13.

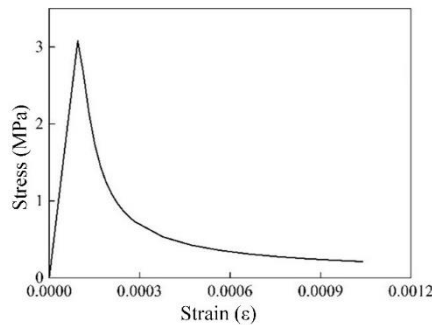


Fig. 13 - Tensile constitutive curve of C40 concrete

### Constitutive Model of Steel Bar

In this paper, the HRB400 type steel bar is adopted as an ideal elastic-plastic material, and the stress-strain curve of steel bar is simulated by using the three-stage curve recommended in the *Code for Design of Concrete Structures* (GB50010-2010), as shown in Figure 14.

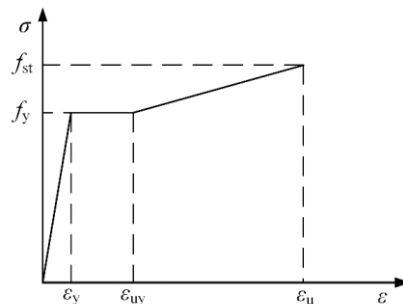


Fig. 14 - Stress-strain curve model of steel bar

## FINITE ELEMENT SIMULATION

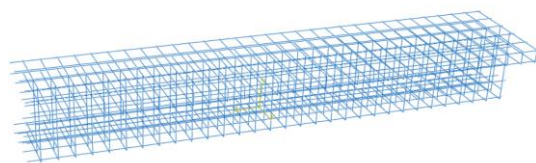
### Finite Element Model

In the ABAQUS finite element model, the concrete was simulated using Soild shape and C3D8R unit, the steel bar was simulated using Wire shape and T3D2truss unit, the bearings and pads were modeled by Soild shape. The concrete model and bearing pad, the concrete model and distribution beam pad, the concrete and the UHPC were all connected with Tie way. The main steel bar and hoop steel bar in the concrete were embedded into the overall model in Embedded way.

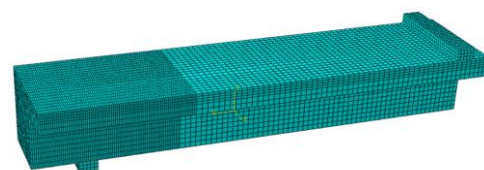
The model adopted four-point loading method, and the model size was consistent with the size of the test beam. The size of the support was  $l \times b \times h = 600 \text{ mm} \times 100 \text{ mm} \times 50 \text{ mm}$ , the center of the support was 200 mm from the end of the beam, the size of the pad at the loading point was  $l \times b \times h = 350 \text{ mm} \times 100 \text{ mm} \times 50 \text{ mm}$ , and the center of the pad was 300 mm from the center line of the beam.

Because of the symmetry of the finite element model, a 1/4 model can be established for analysis and calculation, which can effectively reduce the pressure of the computer running software and improve the speed of model calculation. Figure 15(a) shows the constructed model of the steel reinforcement cage. When applying constraints, applied constraints in X-direction and Z-direction to the X-axis profile and Z-axis profile of the test beam, and added constraints in Y-direction at the support, as shown in Figure 15(b).

In order to help convergence and speed up the calculation, the RP point can be set on the top surface of the pad, and the RP point was coupled with the top surface. The displacement load was applied to the RP point to realize the loading of the test beam. When meshing the test beam, to improve the accuracy of the results, the mesh can be subdivided for the whole area covered by the UHPC of the test beam, and care should be taken to ensure the coupling of the mesh surfaces when meshing. The model meshing is shown in Figure 15(c).



(a) - Model of the steel reinforcement cage



(b) - Model meshing of T-beam

Fig.15 - ABAQUS finite element model

## Comparison of Finite Element Calculation Results with Test Results

### Comparison of Test Results with Finite Element Analysis of Control Beam

Figure 16 shows a comparison of the load-deflection curve of B0 beam measured through test and calculated by finite element software. As can be seen from the comparison diagram, the simulation curve of ABAQUS conforms well to the test curve, which is basically in the overlapping state. In the early stage of loading, the curves all rose linearly. When the load reached 60 kN, the curve of model showed a turning point, cracks began to appear in the beam body, the stiffness of the beam body decreased, and the slope of the load-deflection curve decreased. After that, the load-

deflection curves of the two basically coincided. The ultimate load of B0 beam measured by the test was 280 kN, and the ultimate load calculated by the finite element model was 276 kN, with an error of only 1.4%. It can be considered that the finite element model performed well in simulating the test.

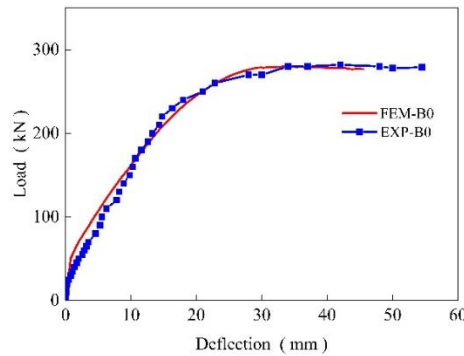


Fig.16 - Comparison diagram of load-deflection curve of Beam B0 between test and finite element

Figure 17(a) shows the tension damage cloud diagram of the beam body simulated by the finite element model. The tension damage of the beam body roughly reflected the distribution and extension direction of cracks. Figure 17(b) shows the cracks diagram of the beam body measured by the test. By comparing the test results with the model calculation, it can be seen that the distribution and development direction of the cracks calculated by the finite element method were roughly similar to the test results. The crack height was roughly 4/5 of the beam height, and the development direction of the cracks all extended to the loading point, and the cracks were mostly near the pure bend section. The closer to the support position, the shorter the fracture length.

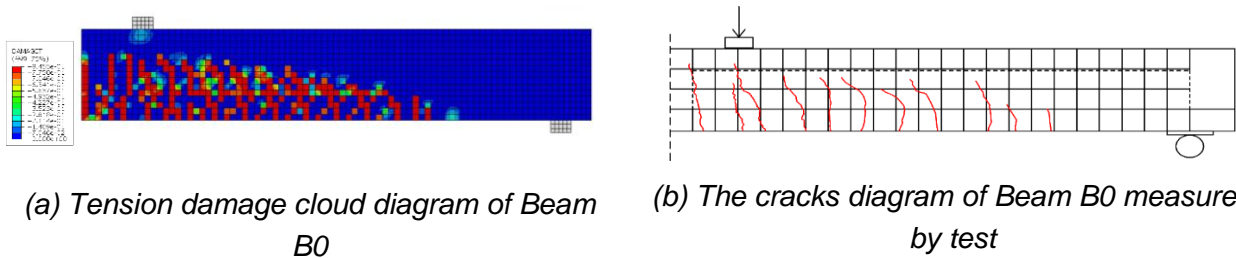


Fig.17 - Comparison of cracks in Beam B0

## Comparison of Test Results with Finite Element Analysis of UHPC Reinforced CCBGSS

Figure 18 shows a comparison of the load-deflection curve of UHPC reinforced CCBGSS measured through test and calculated by finite element software. It can be seen from the figure that the variation of the slope of load-deflection curve in the whole test loading process is basically the same as that in the numerical simulation. In the early stage of loading, the slope of the numerical simulation curve was large, and after reaching a certain load, the slope began to decline. The change of the slope of the curve indicated that the model beam had obvious body damage, that is, the beam body cracks. As the load continued to increase, the numerical simulation curve gradually overlapped with the measured curve. At the late loading stage, the numerical simulation curve and the test curve reached the yield load and the ultimate load almost simultaneously.

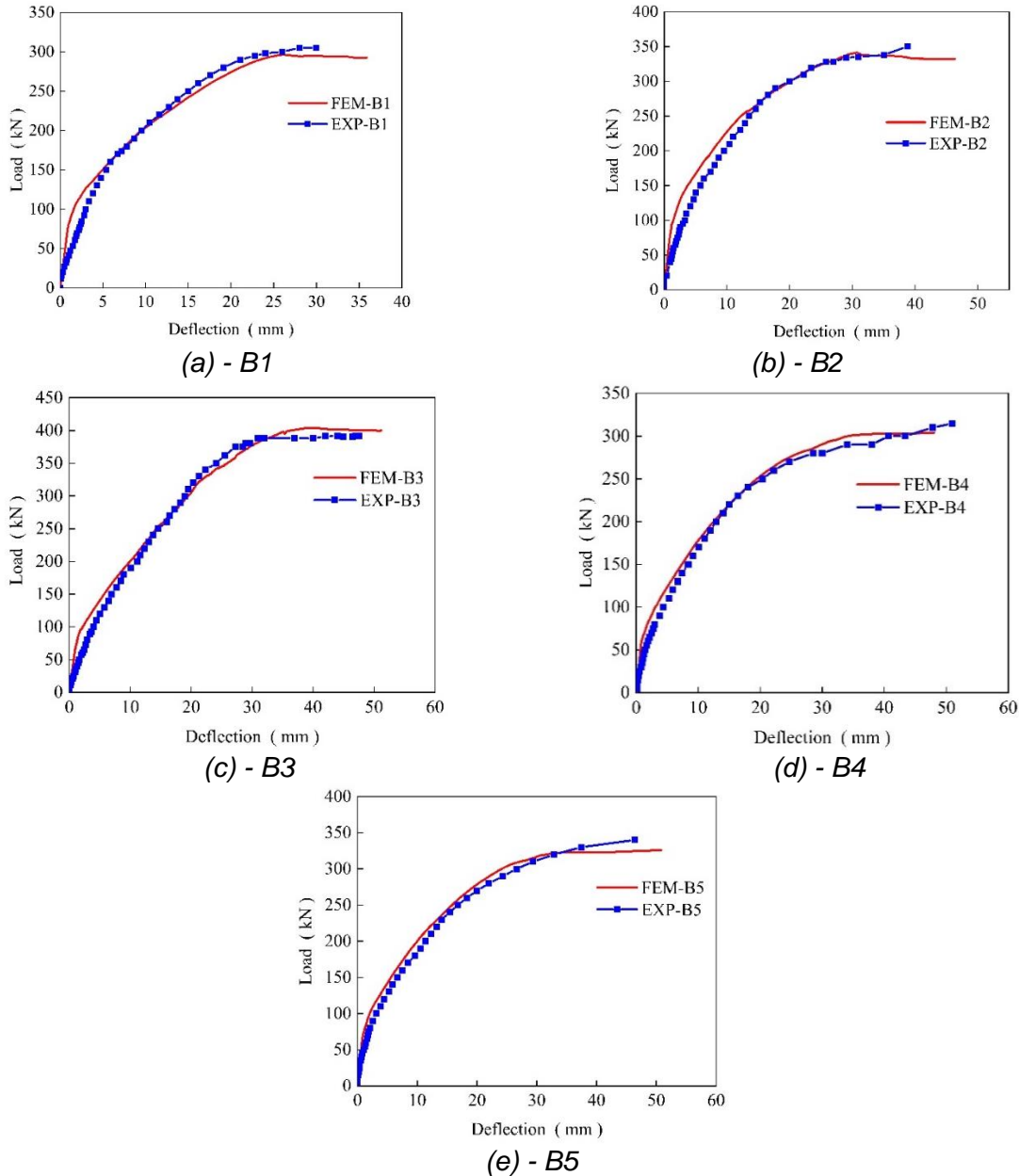


Fig.18 - Comparison diagram of load-deflection curve of UHPC reinforced CCBGSS between test and finite element

The following table is a comparison of the cracking load and ultimate load of the test beam and the finite element model. Among them, the relative error of Beam B4 was the smallest, at 2.0%. The relative error of Beam B2 was the largest, at 8.4%. The relative errors of the cracking load of other beams were all within this error range. In general, the error of cracking load was relatively small, so it can be considered that the finite element model can better simulate the stress behavior of the test beam in the elastic stage, and it also proves that the constitutive relationship curves of concrete and UHPC input in the plastic damage model are in good agreement with the material strength used in the test.

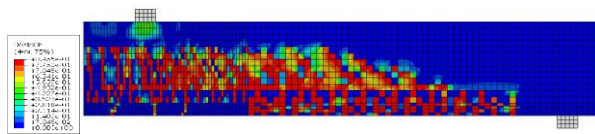
Comparison of results between test beam and finite element model is shown in Table 3. Comparing the ultimate load analysis of the test beams with the finite element model, it can be seen

that the relative error of Beam B3 was the smallest, which was 2.0%. The relative error of Beam B5 was the largest, which was only 4.4%. The relative errors of the ultimate load of other beams were all within this error range. It can be shown that the plastic damage model can better simulate the stress behavior and limit state of the test beam after the yield stage. It also verifies the constitutive relationship of each material and the correctness of the CDP model fitting.

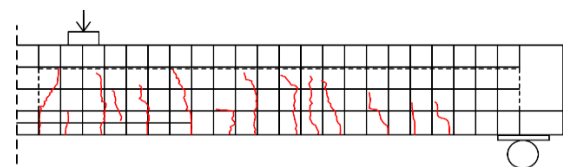
Tab. 3 - Comparison of results between test beam and finite element model

Beam name	Cracking load (kN)		Error	Ultimate load (kN)		Error
	Experimental value	Calculated value		Experimental value	Calculated value	
B1	85	82	3.5%	303	292	3.6%
B2	95	87	8.4%	350	341	2.6%
B3	100	96	4.0%	392	400	2.0%
B4	70	68	2.0%	315	304	3.5%
B5	75	77	2.6%	340	325	4.4%

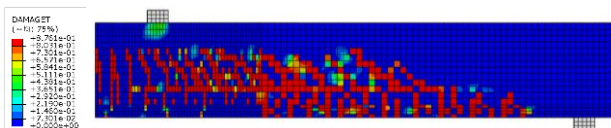
The tensile damage diagrams of the beams calculated by the finite element simulation and the crack distribution diagrams of the beams measured by the test are shown in Figure 19. In the numerical simulation calculation, there were no cracks in the beam body in the elastic stage. When the cracking load was reached, the strain of the beam body increased. Cracks appeared sequentially in the full NC area, interface between UHPC and NC, and the NC and UHPC areas under the UHPC cover. The sequence was basically consistent with the test results. After reaching the yield stage, the damage in the UHPC area increased, eventually showing several cracks that did not penetrate the bottom surface and one crack that extended through the bottom surface to the side. When the load test was carried out to the yield stage of the beam body, the crack distribution in the UHPC region was one macroscopic main crack and many small cracks. The damage morphology of the two was roughly similar, which can indicate that the cracks distribution of finite element numerical simulation is basically consistent with that of test.



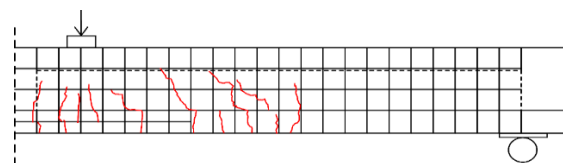
(a) - Tension damage cloud diagram of Beam B1



(b) - The cracks diagram of Beam B1 measured by test



(c) - Tension damage cloud diagram of Beam B2



(d) - The cracks diagram of Beam B2 measured by test

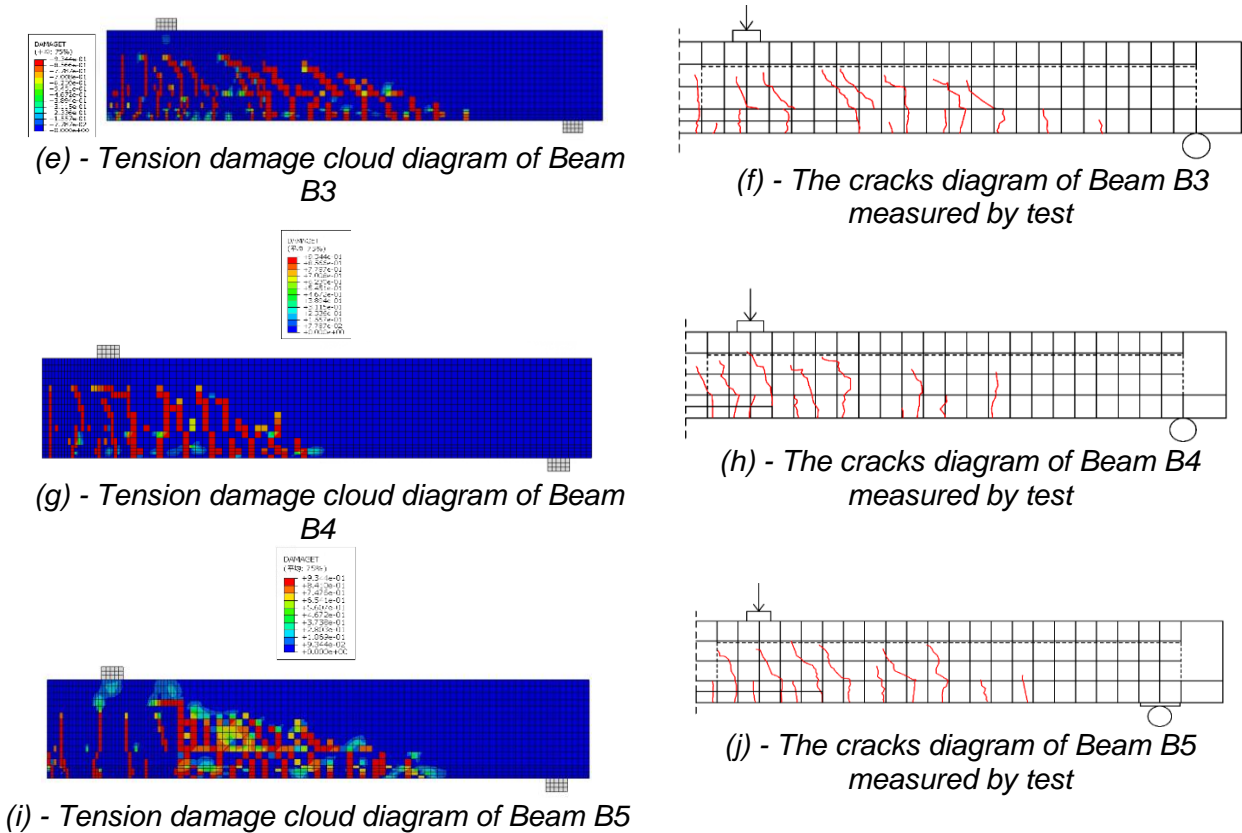
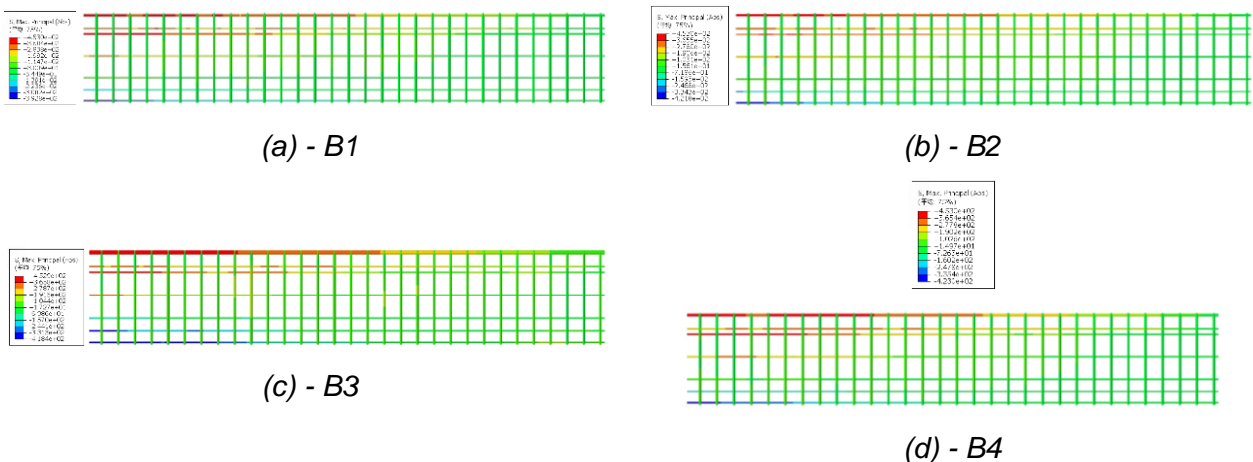
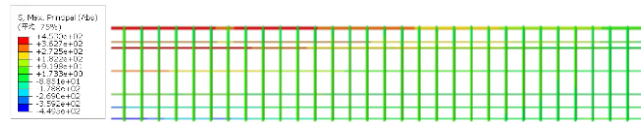


Fig. 19 - Comparison of cracks in UHPC reinforced beams

### Stress Results of UHPC Reinforced CCBGSS

Figure 20 shows the stress cloud diagram of the steel bar of each model test beam when the bearing capacity limit state was reached. It can be seen from the diagram that the stress distribution state of each beam is similar. When the bearing capacity limit state was reached, the main reinforcement in the tension area had reached 453 MPa, indicating that the steel bar in the tension area had yielded. The stress of the stirrups was much less than the yield stress, indicating that the model beams were bending failure, which accorded with the test results.





(e) - B5

Fig. 20 - Stress cloud diagram of steel bar

## Parameter Analysis

Under the condition of ensuring the size and other parameters of the CCBGSS model unchanged, the parameter analysis was further carried out. By changing the pouring thickness and length of UHPC in the negative bending moment zone of CCBGSS, and comparing its load-deflection curve, tensile damage, and stress results, the mechanical properties of UHPC reinforced CCBGSS were explored.

### Different Pouring Thicknesses of UHPC

#### (1) Load-deflection curve

In order to study the influence of different pouring thicknesses of UHPC in the negative moment zone of the CCBGSS on the mechanical properties of the beam, the pouring thicknesses of UHPC in the model were 60 mm, 80 mm and 100 mm, respectively. The sizes of the finite element model were consistent with those of the box girder used in the test. The reinforcement ratio was 0.43%, and the length of UHPC in the negative bending moment zone was 1.6 m. The specific numerical simulation results are shown in Table 4.

Tab. 4 - Numerical simulation results of box girder with different pouring thicknesses of UHPC

Beam number	Pouring thickness of UHPC (mm)	Cracking load (kN)	Increase ratio (%)	Ultimate load (kN)	Increase ratio (%)
FEM-60	60	87	—	341	—
FEM-80	80	94	8.0	351	2.9
FEM-100	100	96	10.3	360	5.6

The cracking load and ultimate load of the CCBGSS increased slightly with the rise of the pouring thickness of UHPC. Taking the model beam with pouring thickness of 60mm as a reference, when pouring thickness increased from 60mm to 80mm and 100mm, the cracking load increased by 8.0% and 10.3%, and the ultimate load increased by 2.9% and 5.6%, respectively.

Figure 21 shows the load-deflection curve of the model beam under different pouring thicknesses of UHPC. As can be seen from the figure, with the increase of load, the development trend of deflection of model beams with different UHPC pouring thicknesses was roughly the same. The curves in the early loading period basically coincided. However, as the load continued to increase, the stiffness of the beam under the same load increased with the rise of pouring thickness, and the bearing capacity also increased.

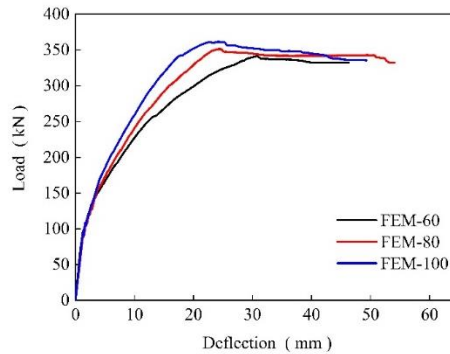


Fig.21 - Load-deflection curve under different pouring thicknesses of UHPC

**(2) Tensile damage cloud diagram**

Figure 22 shows the tension damage cloud diagram of the model beam under different pouring thicknesses of UHPC. Cracks appeared sequentially in the full NC area, interface between UHPC and NC, and the NC and UHPC areas under the UHPC cover. The cracks in the pure bending section basically developed vertically upward, and the cracks in the shear bending section basically developed along the inclined loading point at the bottom of the beam, and the closer the cracks were to the pure bending section, the denser the damage sites were. The cracks in the UHPC area appeared later, and the degree of crack development decreased with the increase of pouring thickness. The cracks in the UHPC area gradually increased after reaching the yield stage, and finally showed several cracks that did not penetrate through the bottom surface and a crack that extended to the side through the bottom surface, which indicated that the negative moment zone of the CCBGSS could effectively limit the development of cracks through the enhancement of the UHPC.

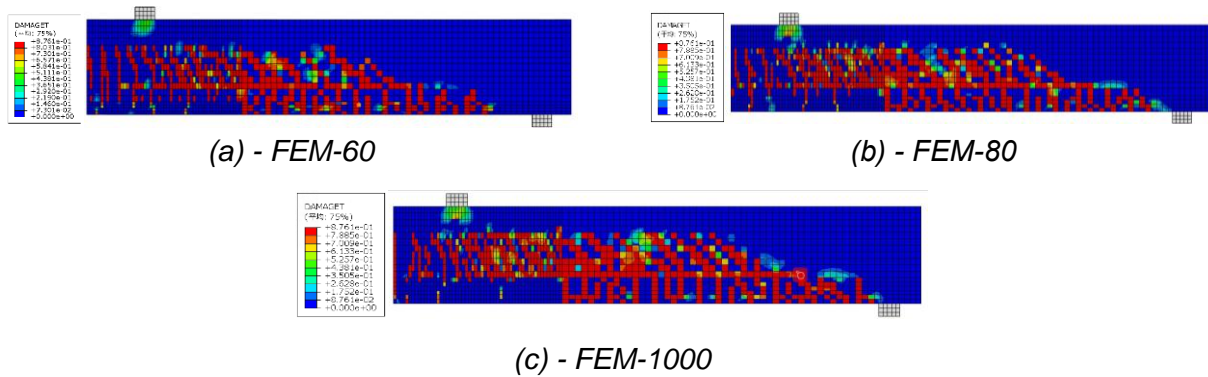


Fig. 22 - Strain damage cloud diagram under different pouring thicknesses of UHPC

**(3) Stress cloud diagram**

Stress cloud diagram of steel bar under different pouring thickness of UHPC is shown in Figure 23. The following figure shows the stress cloud diagram of the steel bar under different thickness of UHPC pouring for CCBGSS. As can be seen from the diagram, when the bearing capacity limit state was reached, the stress of the longitudinal tensile bars of each model beam had reached the original set 453 MPa, and the longitudinal tensile bars had reached the yield state, while the stirrups had not reached the yield strength at this time, which indicated that the model beams

ultimately underwent bending failure.

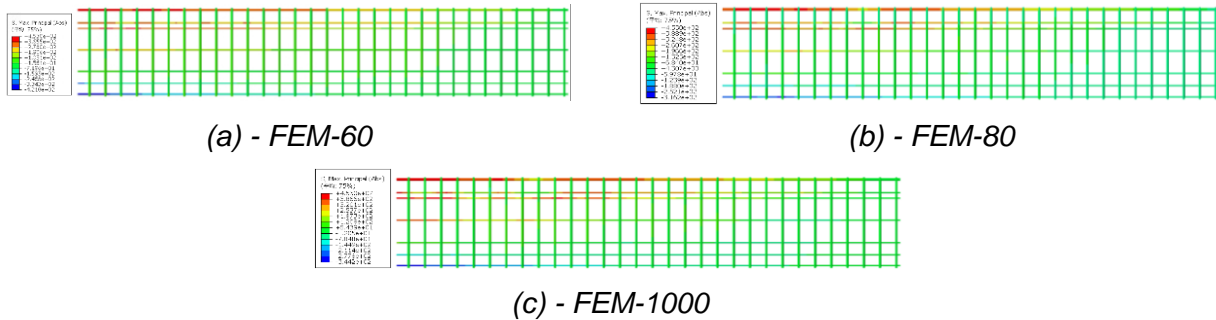


Fig. 23 - Stress cloud diagram of steel bar under different pouring thickness of UHPC

### Different Pouring Lengths of UHPC

In order to study the influence of different pouring lengths of UHPC in the negative moment zone of the CCBGSS on the mechanical properties of the beam, the pouring lengths of UHPC in the model were 1.6 m, 1.8 m, and 2.0 m. The sizes of the finite element model were consistent with those of the box girder used in the test. The pouring thickness of UHPC was 60 mm, the reinforcement ratio was 0.43%. The results of the specific numerical simulation are shown in Table 5.

Tab. 5 - Numerical simulation results of box girder with different pouring thicknesses of UHPC

Beam number	Pouring length of UHPC (m)	Cracking load (kN)	Increase ratio (%)	Ultimate load (kN)	Increase ratio (%)
FEM-1600	1600	87	—	341	—
FEM-1800	1800	96	10.3	352	3.2
FEM-2000	2000	103	18.3	363	6.5

From the above table, it can be seen that the cracking load and ultimate load of the CCBGSS increased with the rise of pouring length of UHPC. Taking the model girder with a pouring length of 1.6 m as a reference, the cracking load was enhanced by 10.3% and 18.3% when the pouring length was increased from 1.6 m to 1.8 m and 2.0 m, respectively, which was a larger enhancement of the cracking load. When the length pouring was increased from 1.6m to 1.8m and 2.0m, the ultimate load was raised by 3.2% and 6.5%, respectively, with a slight increase in ultimate load.

Figure 24 shows the load-deflection curves of the finite element model with different pouring lengths of UHPC. As can be seen from the figure, the load-deflection trend of the model beams was approximately the same, and the curves basically coincided in the early loading period, but as the load continued to increase, the model beam bearing capacity increased with the rise of the pouring length of UHPC.

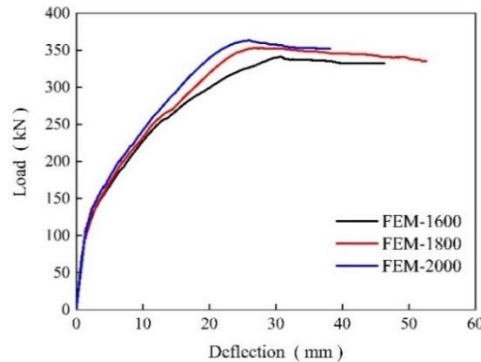


Fig.24 - Load-deflection curve under different pouring lengths of UHPC

## CONCLUSIONS

In this paper, ABAQUS finite element software is used to conduct numerical simulation of UHPC reinforced CCBGSS, and the correctness of the numerical simulation is verified by comparing the model calculation results with the test results. The following conclusions are drawn:

1. Through nonlinear analysis of the finite element model, the results of load-deflection curve, cracking load, ultimate load, stress-strain results and crack development patterns were compared with those measured by the test beam, the following results were obtained:

(1) The variation trend of load-deflection curves measured by the numerical simulation was basically consistent with those measured by the test. The error value of the cracking load of the two was at least 2.0% and at most 8.4%, and the error value of the ultimate load of the two was at least 2.0% and at most only 4.4%, indicating that the finite element model can better simulate the stress behavior of the test beam in the whole process. In practical engineering, finite element software can be used to calculate the stress process of composite beams

(2) The cracks of the beam body appeared in the whole NC region, interface between UHPC and NC, and the NC and UHPC areas covered by UHPC, and the cracks in the model were basically consistent with those measured by the test.

2. The parametric analysis shows that the cracking load and ultimate load of the CCBGSS increased with the rise of thickness and length of UHPC pouring in the negative moment zone. Taking the model beam with pouring thickness of 60 mm as a reference, when the pouring thickness of UHPC increased from 60 mm to 100 mm, the cracking load and ultimate load increased by 10.3% and 5.6% respectively. Taking the model beam with pouring length of 1.6 m as a reference, when the pouring length of UHPC increased from 1.6 m to 2.0 m, the cracking load and ultimate load increased by 18.3% and 6.5% respectively. In practical engineering, the error of cracking load and limit load in finite element simulation is less than 20% and less than 10%, which is reasonable.

## REFERENCES

- [1] Fang, R. , & Yang, X. . 2013. Cause and countermeasure of structure disease of bridge. In ICTIS 2013: Improving Multimodal Transportation Systems-Information, Safety, and Integration, 470-475.
- [2] Liu, H. Y. , Zhao, S. C. , & Li, L. . 2015. Study on bridge deck link slabs of simply supported girder bridges. Advanced Materials Research, 1079, 280-285.

- [3] Du, J. , Meng, W. , Khayat, K. H. , Bao, Y. , Guo, P., Lyu, Z. , & Wang, H. . 2021. New development of ultra-high-performance concrete (UHPC). *Composites Part B: Engineering*, 224, 109220.
- [4] Hung, C. C. , El-Tawil, S. , & Chao, S. H. . 2021. A review of developments and challenges for UHPC in structural engineering: Behavior, analysis, and design. *Journal of Structural Engineering*, 147(9), 03121001.
- [5] Bajaber, M. A. , & Hakeem, I. Y. . 2021. UHPC evolution, development, and utilization in construction: A review. *Journal of Materials Research and Technology*, 10, 1058-1074.
- [6] Ghoneim, G. , & Ghali, A. . 2011. Nonlinear analysis of concrete structures. *Canadian Journal of Civil Engineering*, 9(3), 489-501.
- [7] Dharaneepathy, M. V. , & Anandavalli, N. . 2008. Nonlinear analysis of shock-loaded reinforced concrete structures. *International Journal of Structural Stability & Dynamics*, 4(02), 223-236.
- [8] Shao, X. , Zhou, Y. , Cao, J. , Sun, P. , & Zhu, F. . 2019. Experimental study on flexural behavior of novel continuous deck structure in steel simply-supported beams. *Tumu Gongcheng Xuebao/China Civil Engineering Journal*, 52(12), 80–92.
- [9] Wei, X. , & Peng, D. . 2021. Disease Analysis And Treatment of A Prestressed Concrete Continuous Curved Beam Bridge. In *2021 4th International Symposium on Traffic Transportation and Civil Architecture (ISTTCA)* (pp. 486-490). IEEE.
- [10] Chung, W. , & Sotelino, E. D. . 2006. Three-dimensional finite element modeling of composite girder bridges. *Engineering Structures*, 28(1), 63-71.
- [11] Barth, K. E. , & Wu, H. . 2006. Efficient nonlinear finite element modeling of slab on steel stringer bridges. *Finite elements in analysis and design*, 42(14-15), 1304-1313.
- [12] Rao, Z. , Ning, F. , Li, J. , & Wang, J. . 2020. Experimental study on bending behavior and finite element simulation analysis of glued wood inverted t-beam. *Journal of Engineering Science and Technology Review*, 13(1), 147–159.
- [13] Ling, Q. S. , Tan, J. , Zhai, C. M. , & Li, S. G. . 2014. Simulation analysis of simply-supported T beam bridge with continuous slab-deck structure based on ANSYS. *Applied Mechanics and Materials*, 501–504, 1204–1209.
- [14] Wen-qing, W. , Zhang-xiang, T. , Hui, Z. , & Hao, Z. . 2018. Research on Structural Diseases Due to a Joint Widening of Concrete Continuous Box Girder Bridge. *China Journal of Highway and Transport*, 31(5), 63.
- [15] Wolanski, A. J. . 2004. Flexural behavior of reinforced and prestressed concrete beams using finite element analysis. Milwaukee, Wisconsin.
- [16] Özcan, D. M. , Bayraktar, A. , Şahin, A. , Haktanir, T. , & Türker, T. . 2009. Experimental and finite element analysis on the steel fiber-reinforced concrete (SFRC) beams ultimate behavior. *Construction and Building Materials*, 23(2), 1064-1077.
- [17] Tahmasebinia F. , Ranzi G. . 2011. Three-Dimensional FE Modelling of Simply-Supported and Continuous.Composite Steel-Concrete Beams[J]. *Procedia Engineering*, 14(2259):434-441.
- [18] Yu, R. , Spiesz, P. , & Brouwers, H. J. H. . 2014. Mix design and properties assessment of ultra-high performance fibre reinforced concrete (UHPRFC). *Cement and concrete research*, 56, 29-39.
- [19] Azmee, N. M. , & Shafiq, N. . 2018. Ultra-high performance concrete: From fundamental to applications. *Case Studies in Construction Materials*, 9, e00197.
- [20] Kwon, S. , Nishiwaki, T. , Kikuta, T., & Mihashi, H. . 2014. Development of ultra-high-performance hybrid fiber-reinforced cement-based composites. *ACI Materials Journal*, 111(3), 309.
- [21] Moosa, M. K. , & Ali, A. Y. . 2023. Experimental investigation on the transform the simply supported girders to continuous girder by using the UHPC cast in place joint. *KSCE Journal of Civil Engineering*, 27(4), 1697-1707.
- [22] Graybeal, B. A. . 2010. Behavior of field-cast ultra-high performance concrete bridge deck connections under cyclic and static structural loading (No. FHWA-HRT-11-023). United States. Federal Highway Administration.
- [23] GB 50010-2010, Code for Design of Concrete Structures [S].